Ultrathin, flexible, solid polymer composite electrolyte enabled with aligned nanoporous host for lithium batteries

Jiayu Wan[1,6], Jin Xie[1,2,6], Xian Kong[3], Zhe Liu[4], Kai Liu[1], Feifei Shi[1], Allen Pei[1], Hao Chen[1], Wei Chen[1], Jun Chen[1], Xiaokun Zhang[1], Linqi Zong[1], Jiangyan Wang[1], Long-Qing Chen[4], Jian Qin[3] and Yi Cui[1,5]*

The urgent need for safer batteries is leading research to all-solid-state lithium-based cells. To achieve energy density comparable to liquid electrolyte-based cells, ultrathin and lightweight solid electrolytes with high ionic conductivity are desired. However, solid electrolytes with comparable thicknesses to commercial polymer electrolyte separators (~10 μm) used in liquid electrolytes remain challenging to make because of the increased risk of short-circuiting the battery. Here, we report on a polymer–polymer solid-state electrolyte design, demonstrated with an 8.6-μm-thick nanoporous polyimide (PI) film filled with polyethylene oxide/lithium bis(trifluoromethanesulfonyl)imide (PEO/LiTFSI) that can be used as a safe solid polymer electrolyte. The PI film is nonflammable and mechanically strong, preventing batteries from short-circuiting even after more than 1,000 h of cycling, and the vertical channels enhance the ionic conductivity (2.3×10^{-4} S cm^{-1} at 30 °C) of the infused polymer electrolyte. All-solid-state lithium-ion batteries fabricated with PI/PEO/LiTFSI solid electrolyte show good cycling performance (200 cycles at C/2 rate) at 60 °C and withstand abuse tests such as bending, cutting and nail penetration.

Lithium (Li)-ion batteries (LIBs) are ubiquitously recognized as the dominant energy storage device[1–4]. In pursuit of LIBs with better performance, tremendous progress has been made on every component in batteries[5–8]. However, the dilemma of high performance versus safety of LIBs remains a problem, leading to catastrophic battery incidents. The ever-increasing demand for high-energy-density LIBs urges the utilization of the ultimate metallic Li anode, which further complicates safety issues[9–12]. Li dendrites formed during electrochemical Li plating and stripping can penetrate the separator, leading to battery short-circuiting, and eventually fire and tragedies.

To address the aforementioned safety concerns, solid-state electrolytes (SSEs) have attracted great attention as replacements for the flammable liquid electrolyte in current LIBs[13–15]. Ideally, SSEs should be highly ionically conductive, mechanically strong, nonvolatile, nonflammable and chemically/electrochemically stable within the battery operation window. To date, numerous studies have been carried out to investigate different types of SSE materials for safer LIBs[16,17]. These SSEs can be summarized in three categories: inorganic (ceramic/glass) solid electrolytes[18–20], solid polymer electrolytes (SPEs)[21,22] and their hybrids[23,24]. Inorganic SSEs generally have the highest ionic conductivity among all types of SSEs, with some (sulfide superionic conductors) even exceeding that of liquid electrolytes[20]. Recent studies addressing the notoriously large interfacial resistance of Li/inorganic SSEs have given inorganic SSEs a giant leap towards their application in LIBs[18,25]. However, the brittle nature of inorganic SSE pellets may greatly hinder their processability and use in practical applications such as in electrical vehicles, where even a small bump may cause structural failure. Inorganic SSEs are also not flexible and are relatively thick (>200 μm) to preserve their intact structure during handling. Recent findings have revealed an intrinsic high electronic conductivity in certain inorganic SSEs, especially at grain boundaries, leading to hazardous direct Li deposition inside of them[26,27]. The above issues must therefore be addressed before utilizing inorganic SSEs in commercial all-solid-state batteries[28].

SPEs are mainly composed of uniform mixtures of solid polymers and Li salts. These SSEs are widely studied due to their high flexibility, light weight, low cost and easy scalability. However, the intrinsic softness of these polymer systems and their moderate ionic conductivity hinder the use of pure polymer/Li salt composites in LIBs[29,30]. In the most-studied system of polyethylene oxide (PEO), adding plasticizers or grafting functional branches to PEO chains can enhance the ionic conductivity and modulus of the SPE. Even so, PEO itself is still flammable, making its SPEs similarly unfavourable compared with liquid electrolytes. The marriage of organic and inorganic solid electrolytes into a composite solid electrolyte is promising because it improves ionic conductivity without sacrificing the flexibility of the polymer electrolyte[31–35]. The enhanced ionic conductivity arising from aligned composite polymer–inorganic SPE structures furthers the advantages of these SSEs[36,37]. A previous report showed that aligning Li conducting ceramic nanowires in a horizontal configuration can improve ionic conductivity in polyacrylonitrile/$LiClO_4$ polymer electrolyte systems[24]. Nevertheless, even with state-of-the-art SSE systems, it is extremely difficult to create high-ionic-conductivity (>10^{-4} S cm^{-1}), thin SSEs (<10 μm) at room temperature by positioning inorganic components in a vertical configuration, while simultaneously obtaining stable cycling performance within a full battery. If such an SSE design was available,

[1]Department of Materials Science and Engineering, Stanford University, Stanford, CA, USA. [2]School of Physical Science and Technology, ShanghaiTech University, Shanghai, China. [3]Department of Chemical Engineering, Stanford University, Stanford, CA, USA. [4]Department of Materials Science and Engineering, The Pennsylvania State University, University Park, PA, USA. [5]SLAC National Accelerator Laboratory, Stanford Institute for Materials and Energy Sciences, Menlo Park, CA, USA. [6]These authors contributed equally: Jiayu Wan, Jin Xie. *e-mail: yicui@stanford.edu

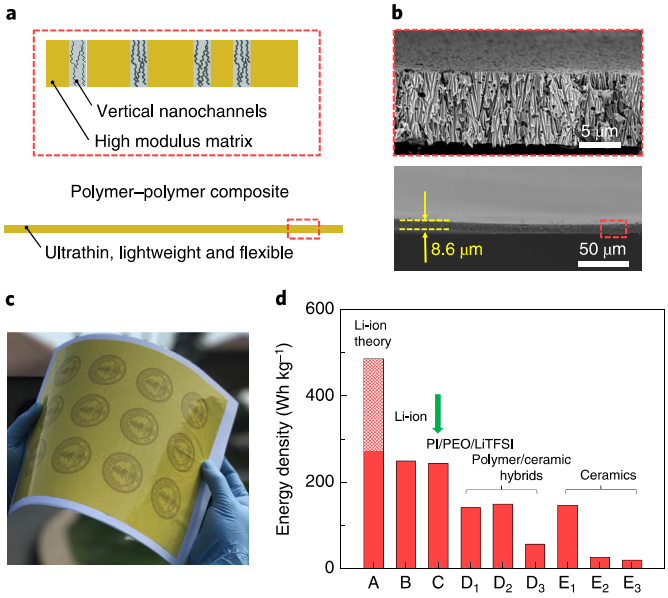

Fig. 1 | Design of polymer–polymer composite SSE. a, Schematic showing the design principles of our polymer–polymer composite SSE. **b**, Cross-sectional SEM images of an ultrathin nanoporous PI film (bottom) with zoomed-in image of the aligned nanopores (top). **c**, Photo image of a large-scale porous PI film. **d**, Energy density chart of batteries where different electrolytes, battery casings, separators and liquid/solid electrolytes are all taken into account. D_1–D_3 denote polymer/ceramic composite SSEs, where D_1 and D_2 are $Li_7La_3Zr_2O_{12}$ (LLZO)/PEO/LiTFSI composite and D_3 is SiO_2/PEO/$LiClO_4$ composite; E_1–E_3 denote ceramic-type SSEs, where E_1 is ultrathin LLZO, E_2 is regular $Li_{10}GeP_2S_{12}$(LGPS)-type SSE and E_3 is regular LLZO. See Supplementary Table 1 and Supplementary Fig. 2 for details.

it would potentially lead to high-ionic-conductivity, high-energy-density and safe all-solid-state LIBs.

Here, we propose the design of an ultrathin, high-performance polymer–polymer composite solid electrolyte for all-solid-state Li batteries. (Fig. 1a) The composite SSE is made of a robust, non-flammable host with vertically aligned nanochannels and Li-ion conductive SPE fillers. The high modulus host prevents potential dendrite penetration while the aligned channels enhance the ionic conductivity of SPE fillers. The ultrathin and polymer–polymer nature of the composite electrolyte enables great flexibility, low electrolyte resistance and potential high energy density of a full battery.

High modulus, nanoporous polyimide (PI) hosts and PEO/lithium bis(trifluoromethanesulfonyl)imide (LiTFSI) polymer electrolytes are utilized as a proof-of-concept polymer–polymer SSE for our design (see also Supplementary Fig. 1). Cross-sectional scanning electron microscopy (SEM) images of the ultrathin, porous PI matrix are shown in Fig. 1b, where the thickness is identified to be 8.6 μm (Fig. 1b, bottom). The vertical nanoporous morphology of PI is zoomed in and shown in Fig. 1b (top). A photo image of a large-scale, nanoporous and flexible PI film on a white paper is shown in Fig. 1c, demonstrating the scalability of such a composite system. We compare the energy densities of state-of-the-art commercial LIBs with both standard liquid electrolyte and various solid electrolytes in Fig. 1d, to illustrate the advantage of our polymer–polymer SPE. Although the theoretical energy density of the commercial LIB approaches 480 Wh kg^{-1}, it decreases by about half when the metal casing, cathode current collector (Al) and anode current collector (Cu) are considered in the calculation (column A). The energy density further decreases when separators and liquid electrolyte are taken into consideration (column B). However, the energy densities of all-solid-state cells are comparable to those of liquid electrolyte cells when our PI/PEO/LiTFSI electrolyte is utilized (246 Wh kg^{-1}), and much higher than other state-of-the-art all-solid-state batteries (more details in Supplementary Table 1 and Supplementary Fig. 2). The thin, ultralight PI/PEO/LiTFSI obtains a similar area density (1.12 mg cm^{-2}) to separator/liquid electrolyte (1 mg cm^{-2}), ensuring its advantage over other solid electrolyte systems (see also Supplementary Fig. 2). Energy densities of solid polymer–polymer composite LIBs could potentially reach the pink area in column A, as cell casing for all-solid-state LIBs could be simpler than LIBs with liquid electrolytes. Even higher energy densities could potentially be realized through high-capacity Li chemistries, such as sulfur and metallic lithium.

Characterizations of PEO/LiTFSI in porous PI

SEM images before and after the infiltration of PEO/LiTFSI polymer electrolyte into the PI film are presented in Fig. 2a–d. Figure 2a shows a top-view image of the porous PI film in which the pores are uniformly distributed (zoomed-out image in Supplementary Fig. 3) with diameters of around 200 nm. These images show that the pores occupy about 11% of the area on the PI surface. After PEO/LiTFSI infiltration, the pores are completely filled with PEO/LiTFSI and serve as the Li-ion conductive medium (Fig. 2b). Cross-sectional SEM images of the porous PI film (Fig. 2c) and filled PI/PEO/LiTFSI film (Fig. 2d) also demonstrate the complete infiltration of PEO/LiTFSI in the vertical pores. The ionic conductivities of the SSEs were measured using blocking cells from −20 to 100 °C. The PEO/LiTFSI in the PI vertical channels is measured to have enhanced ionic conductivity compared with that of PEO/LiTFSI thin film across all measurement temperatures (Fig. 2e and Supplementary Figs. 4–6). Specifically, the PEO/LiTFSI in aligned channels shows ionic conductivity of 2.3×10^{-4} S cm^{-1} at 30 °C, whereas the PEO/LiTFSI thin film only shows conductivity of 5.4×10^{-5} S cm^{-1} (30 °C). The electrochemical impedance spectroscopy curves of PI/PEO/LiTFSI at different temperatures are plotted in Fig. 2f.

To investigate the effect that the vertical channels may have on PEO/LiTFSI, we conducted a two-dimensional X-ray diffraction characterization of the PEO/LiTFSI electrolyte and PEO/LiTFSI filled in vertically aligned 200 nm channels. In Fig. 2g,h, the ring diffraction patterns (indicated with blue and green arrows) that appear in the composites are attributed to the (120) and (112) planes of the PEO crystallites, respectively. The PEO/LiTFSI thin-film sample shows an isotropic ring pattern (Fig. 2g), revealing an isotropic distribution of the crystallites. In contrast, Fig. 2h shows the PEO/LiTFSI in the vertical channels with a concentrated intensity on the *y* axis, which represents a textured distribution of crystallites along the out-of-plane direction. This indicates that the channels inside the matrix help align the PEO crystallites along them (for more details see Supplementary Fig. 7). Recent reports also show that similar alignment effects on polymers leads to thermal or ionic transport enhancement in the aligned direction, both of which are related to vibration of polymer chains[38,39].

We then carried out molecular dynamics simulations to explore the reason for enhanced ionic conductivity. In our simulations, PEO/LiTFSI with random and aligned polymer chains are compared to show the difference in Li ionic conductivity. The simulation snapshots of the two systems are shown in Fig. 2i (PEO with randomly oriented chains and Li salts) and Fig. 2j (PEO with aligned chains and Li salts). Mean squared displacements (MSDs) of Li ions in both aligned and random PEO matrices at 350 K are calculated and displayed in Fig. 2k. The MSDs in different directions for the random-chain PEO system show little difference and the values are comparable to literature results[40,41]. In contrast, we found a clear increase in Li^+ diffusion along the aligned direction (*z*) compared with all directions from the randomly oriented PEO/LiTFSI sample. The ionic diffusion along the aligned direction shows an even bigger difference to those in the other two directions (*x* and *y*) in

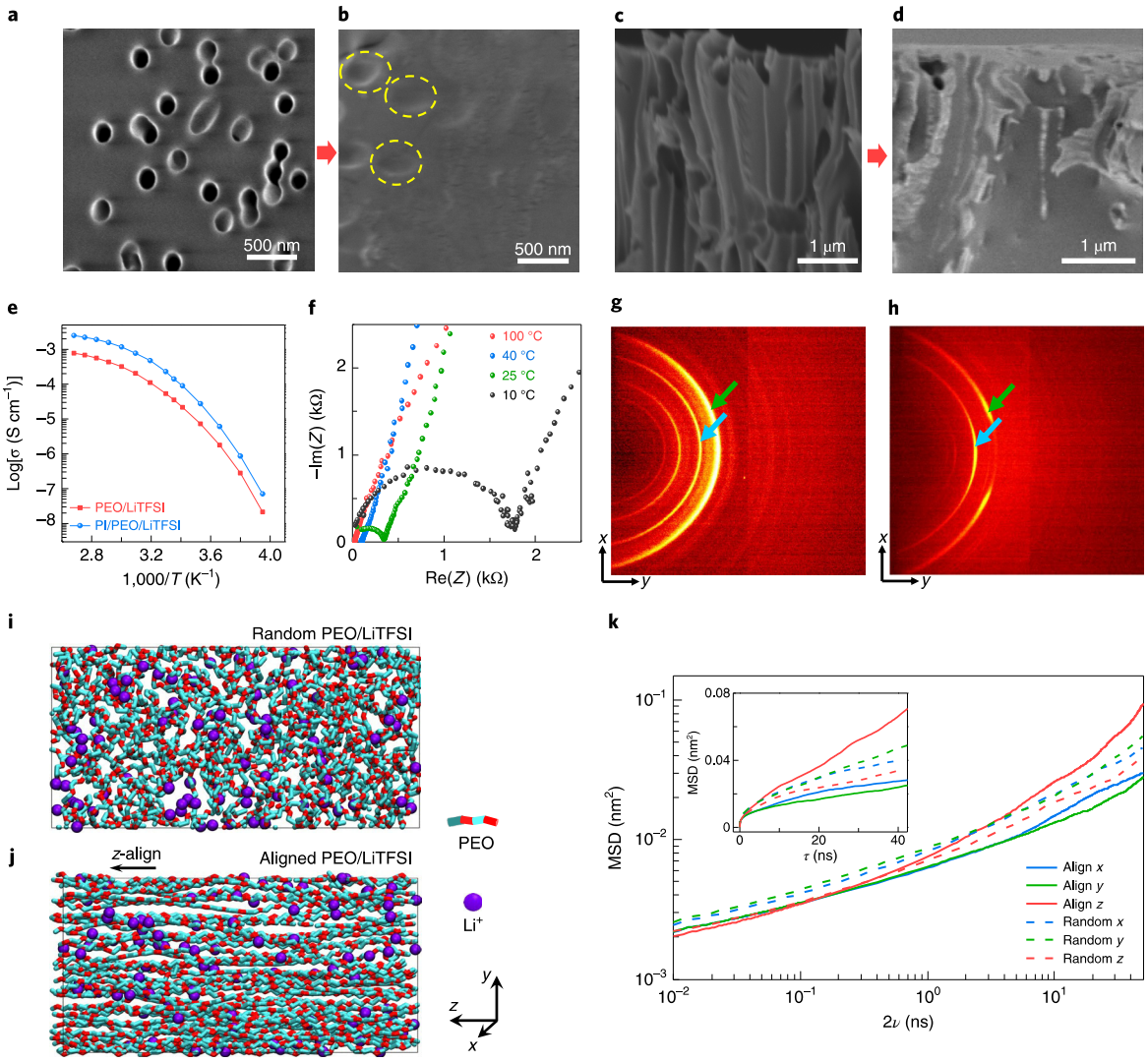

Fig. 2 | Characterization and understanding of PEO/LiTFSI in aligned channels. a,**b**, SEM image (from top view) before (**a**) and after (**b**) PEO/LiTFSI infiltration into the porous PI film. The yellow dashed circles highlight the pores that are filled by PEO/LiTFSI. **c**,**d**, SEM image (from side view) before (**c**) and after (**d**) PEO/LiTFSI infiltration in porous PI film. **e**, Arrhenius ionic conductivity (σ) plots of PEO/LiTFSI thin-film SPE and PEO/LiTFSI within PI/PEO/LiTFSI SPE. **f**, Selected temperature-dependent electrochemical impedance spectroscopy plots of PI/PEO/LiTFSI SPE. **g**,**h**, Two-dimensional wide-angle X-ray diffraction plots of a PEO/LiTFSI thin film (**g**) and PEO/LiTFSI infiltrated in an anodic aluminium oxide template with 200-nm-diameter pores. The blue and green arrows indicate the different planes of the PEO crystallites. (**h**). **i**,**j**, Simulation model of Li^+ transport in a random system (**i**) and *z*-aligned PEO system (**j**). $TFSI^-$ ions are not shown in the schematics. **k**, MSD versus diffusion time (τ) of Li transport in random and aligned PEO systems on log scale. Inset: the same plot on linear scale.

the aligned PEO/LiTFSI system. Based on our simulation results, Li ions find the best diffusion path along the alignment direction. The diffusion coefficients for each system are calculated based on the slope of the MSD between 25 ns and 35 ns (inset of Fig. 2k). The diffusivity of the aligned *z* direction is $1.3\times10^{-8}\,cm^2\,s^{-1}$, while the average diffusivity in the random system is only $5.7\times10^{-9}\,cm^2\,s^{-1}$. Our molecular dynamics simulations show that polymer-chain alignment is beneficial to ion diffusion in the alignment direction, providing a possible explanation for the enhanced ionic conductivity of PI/PEO/LiTFSI in the aligned channels. This explanation is consistent with previous reports of stretching-induced ionic conductivity enhancement in polymer electrolytes[42]. This ionic conductivity enhancement of PEO/LiTFSI in aligned nanochannels may be attributed to the nanoconfinement effects of channels and/or polymer-chain alignment at SPE/channel interfaces[24,30,43]; other advanced techniques, such as solid-state NMR[37] or neutron depth profiling[44], may be able to more thoroughly characterize the contributing factors of this effect in the future.

Electrochemical tests of PI/PEO/LiTFSI electrolyte

We then made Li/SPE/Li symmetric cells to evaluate the mechanical stability of the PI/PEO/LiTFSI SPE during the Li plating and stripping process. The cycling tests were carried out at 60 °C, as shown in Fig. 3a (zoomed-in plot shown in inset; see also Supplementary Fig. 8 and more Li–Li tests in Supplementary Figs. 9–11). Under a current density of $0.1\,mA\,cm^{-2}$, a hard short occurred in a very short time (less than 40 h) in plain PEO cells. Despite the PEO/LiTFSI thin film being much thicker (130 μm) than the ultrathin PI/PEO/LiTFSI SPE, the latter demonstrated much stabler performance during Li plating and stripping, lasting 1,000 h at 60 °C. Stress–strain curves of PEO/LiTFSI and porous PI obtained through tensile tests are plotted in Fig. 3b. The porous PI shows a much larger modulus of

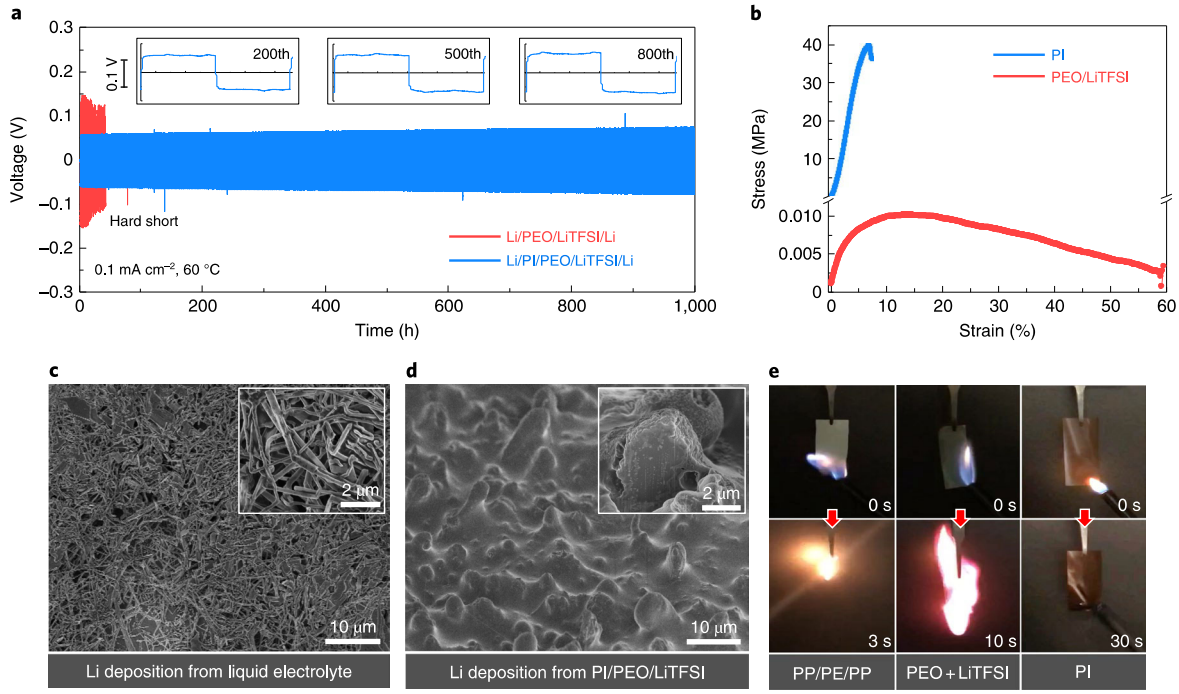

Fig. 3 | Mechanical and fire-retarding properties of PI/PEO/LiTFSI. a, Long-term cycling of symmetrical Li–Li cells with PEO/LiTFSI thin-film electrolyte and PI/PEO/LiTFSI SPE electrolyte at 60 °C. Inset: voltage profile of Li/PI/PEO/LiTFSI/Li at the 200th, 500th and 800th hours, respectively. Each cycle lasts for 1 h. **b**, Stress–strain curve of porous PI film versus PEO/LiTFSI (EO:Li = 10:1) film. **c**,**d**, SEM images showing Li deposition morphology on Cu with liquid electrolyte (**c**; inset shows typical zoomed-in SEM image of **c**) and PI/PEO/LiTFSI solid electrolyte (**d**; inset shows one of the protrusions cut by a focused ion beam). **e**, Photo images of flame test on a regular PP/PE/PP (PP, polypropylene; PE, polyethylene) separator, a PEO/LiTFSI film and a PI film.

850 MPa, which is almost five orders of magnitude higher than that of PEO/LiTFSI (only 0.1 MPa). Figure 3c,d compares the Li deposition morphology with EC/DEC/$LiPF_6$ liquid electrolyte (EC, ethylene carbonate; DEC, diethyl carbonate) and PI/PEO/LiTFSI SPE (under the same Li plating conditions), respectively. Obvious dendrite formation is observed with the liquid electrolyte, while only suppressed Li protrusion formation is observed with the PI/PEO/LiTFSI SPE. Note that the Li protrusions under PI/PEO/LiTFSI have diameters of a few micrometres, in contrast to dendrites of a few hundred nanometres from EC/DEC/$LiPF_6$. This phenomenon indicates that the deposited Li does not tend to penetrate the soft channel region, but rather pushes forward the composite electrolyte as a whole. The suppressed Li dendrite growth results from the increased modulus of the PI/PEO/LiTFSI SPE, explaining the long, durable performance and stability of PI/PEO/LiTFSI SPE during Li stripping/plating (see also Supplementary Figs. 10–20). This success also indicates the potential of the proposed high-modulus-matrix/high-ionic-conductivity filler structures to prevent dendrite formation. Moreover, the PI host is flame retardant, whereas pure PEO/LiTFSI ignites easily (Fig. 3e; see also Supplementary Videos 1–3, for more details).

Finally, we tested the PI/PEO/LiTFSI film as a SSE in all-solid-state LIBs. The coin cells were made with $LiFePO_4$ (LFP) cathodes, PI/PEO/LiTFSI as the solid electrolytes and Li metal as the anodes. Control cells were made with the same cathodes and anodes, but using PEO/LiTFSI as the solid electrolytes instead. The thickness of PEO/LiTFSI is around 150 μm to prevent short circuits during cycling at initial stages. The PI/PEO/LiTFSI cells were tested at 60 °C and delivered excellent rate performance. Voltage profiles (Fig. 4a) at different rates show clear plateaus at around 3.45 V, which is typical for LFP cathodes. Note that the ultrathin PI/PEO/LiTFSI cell maintains very low overpotentials of 55 mV and 42 mV at C/5 and C/10 rates, respectively. Even at C/2, the overpotential of LFP/PI/PEO/LiTFSI/Li is only 100 mV, reflecting the thin nature of the PI/PEO/LiTFSI film. In contrast, a relatively large overpotential of 86 mV is observed at C/10 for LFP/PEO/LiTFSI/Li. When cycling these cells at C/10, C/5, C/2 and 1 C, the LFP/PI/PEO/LiTFSI/Li all-solid-state LIB delivered high specific capacities of 176 mAh g^{-1}, 156 mAh g^{-1}, 138 mAh g^{-1} and 125 mAh g^{-1}, respectively (Fig. 4b). The LFP/PI/PEO/LiTFSI/Li cell also shows very stable cycling for more than 200 cycles at C/2, whereas the LFP/PEO/LiTFSI/Li cell decays dramatically within 100 cycles (Fig. 4c). We similarly demonstrated that the LFP/PI/PEO/LiTFSI/Li cells can be stably cycled at lower temperatures of 40 °C and 30 °C with capacity larger than 120 mAh g^{-1}. When a lower molecular weight PEO (MW = 10,000, polymer–polymer solid electrolyte defined as PI/PEO_{10}/LiTFSI) is used, the LFP/PI/PEO_{10}/LiTFSI/Li can be cycled at 30 °C and still obtains a stable specific capacity of 100 mAh g^{-1} at a fast charging rate of C/2 (Fig. 4d,e; for more cycling performance results see also Supplementary Figs. 21–24). In summary, we have made and tested a SSE with vertically aligned structures in a full-cell configuration.

Abuse tests of PI/PEO/LiTFSI in full cells

After folding and unfolding, the PI/PEO/LiTFSI SPE was able to regain its original shape and functioned properly within a LFP/PI/PEO/LiTFSI/Li coin cell (Fig. 5a,b). Pouch-type cells of LFP/PI/PEO/LiTFSI/Li were made to verify the flexibility of the all-solid-state LIB. As shown in Fig. 5c, the all-solid-state pouch cell is connected to a red light-emitting diode (LED). When twisted or folded, the LED remained lit, demonstrating the good flexibility of the PI/PEO/LiTFSI all-solid-state battery. Abuse tests such as nail tests and cutting tests were also carried out with pouch-type LFP/PI/PEO/LiTFSI/Li all-solid-state batteries. After the nail test (Fig. 5d; see also Supplementary Video 4), the solid-state pouch cell not only stays safe (unlike typical LIBs, which often violently combust after such abuse) but also remains operational (shortly afterwards) and

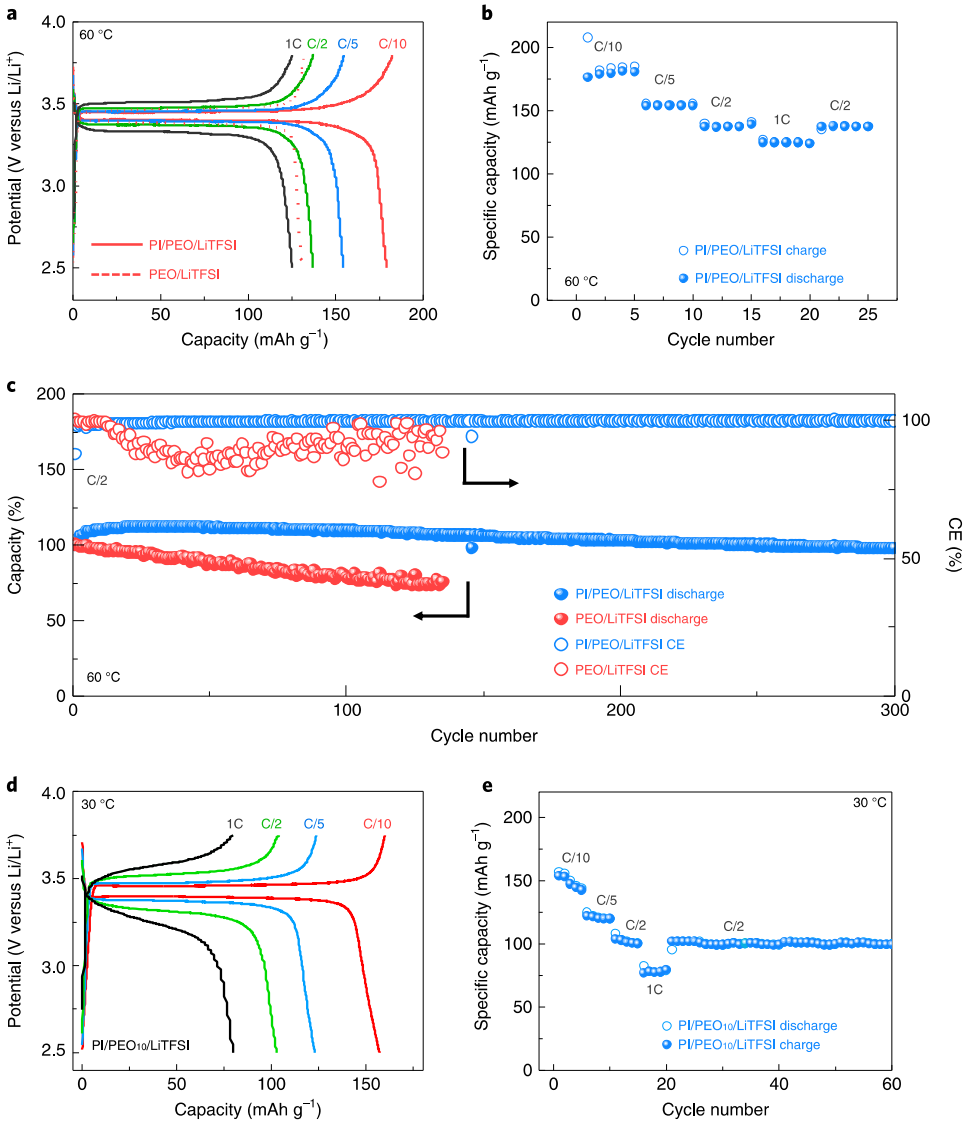

Fig. 4 | Full-cell performance with PI/PEO/LiTFSI-based batteries. a, Voltage profile of a Li/PI/PEO/LiTFSI/LFP cell at different charging rates, cycled at 60 °C. Red dashed line is the Li/PEO/LiTFSI/LFP cell at C/10, at 60 °C. **b**, Cycling performance of a Li/PI/PEO/LiTFSI/LFP cell at different charging rates, cycled at 60 °C. **c**, Capacity retention performance of Li/PI/PEO/LiTFSI/LFP and Li/PEO/LiTFSI/LFP cells at C/2, cycled at 60 °C. CE, Coulombic efficiency. **d**,**e**, Voltage profile (**d**) and cycling performance (**e**) of a Li/PI/PEO_{10}/LiTFSI/LFP cell at different charging rates, cycled at 30 °C.

lights up the LED bulb. The PI/PEO/LiTFSI pouch cell can also still light up the LED even after the cell is cut in half.

Compared with other types of SSEs, the ultrathin nature of the polymer–polymer hybrid SSE leads to a uniquely high energy density. The processability and flexibility of polymer or composite SSEs makes it attractive to pair them with current LIB production. However, although the ionic conductivities of composite type SSEs are comparable to some of the ceramic SSEs (such as garnet type SSE, ~10^{-4} S cm^{-1} at room temperature), they are still behind those of sulfide-based SSEs (10^{-3}–10^{-2} S cm^{-1}) and liquid electrolyte cells (~10^{-2} S cm^{-1}). Thus, battery performance with composite electrolytes cycling at high current density at moderate (25–40 °C) temperature is still not sufficient. Future research to improve the performance of composite SSEs should focus on: (1) further enhancing their intrinsic ionic conductivities; (2) increasing effective ionic conduction pathways (such as adding more ion-conducting channels) in the SSE; (3) lessening the interphase resistance (cathode/electrolyte, anode (Li metal)/electrolyte); (4) using mechanically strong, chemically/electrochemically stable materials (at least can be stabilized at the electrolyte/electrode interface) to obtain composite SSEs with reduced thickness, while remaining able to prevent short-circuiting of the battery; and (5) designing smart battery configurations to run batteries at elevated temperature with minimum energy loss through thermal conduction.

Conclusions

We have demonstrated a polymer–polymer SSE with an ultrathin, flexible, mechanically strong, nonflammable and porous PI film as the host and PEO/LiTFSI as the ionically conducting filler. Compared with conventional PEO/Li salt-based SPEs, the hybrid electrolyte has five orders of magnitude higher modulus and enhanced ionic conductivity. Thus, the hybrid PI/PEO solid electrolyte demonstrates cycling stability superior to that of plain PEO in Li/SPE/Li cells under identical current density. Furthermore, in LFP/SPE/Li full cells, the rate performance and cycling stability of the PI/PEO/LiTFSI SPE is also better than that of PEO/LiTFSI. LFP/PI/PEO/LiTFSI/Li all-solid-state pouch cells also demonstrate high tolerance to abuses such as bending, twisting, cutting and nail perforation.

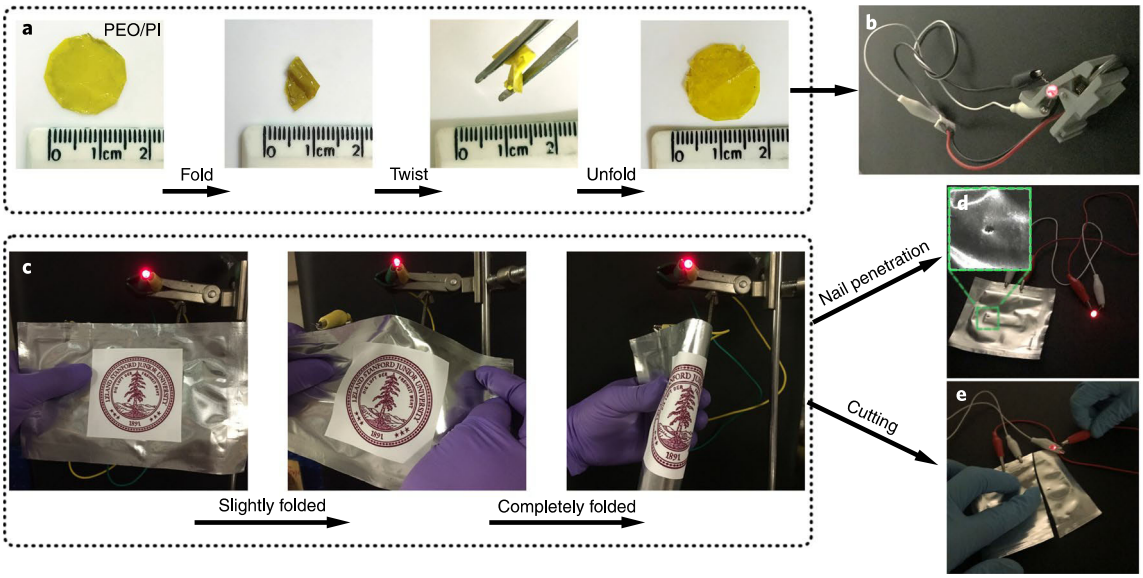

Fig. 5 | Abuse tests of PI/PEO/LiTFSI. a, Photo images of 2 cm^2 PI/PEO/LiTFSI SSE free-standing film being abused via folding, twisting and unfolding. **b**, Photo image of the abused PI/PEO/LiTFSI film as a SSE in a LFP/PI/PEO/LiTFSI/Li coin cell lighting a LED bulb. **c**, Flexible Li/PI/PEO/LiTFSI/LFP pouch cell lighting a LED bulb. **d**, Li/PI/PEO/LiTFSI/LFP pouch cell lighting a LED bulb after nail test. **e**, Li/PI/PEO/LiTFSI/LFP pouch cell lighting a LED bulb after cutting.

Thus, the proposed polymer–polymer composite SPE configuration represents a promising route to make LIBs that are safe, high energy density, high performing and flexible.

References

1. Armand, M. & Tarascon, J. M. Building better batteries. *Nature* **451**, 652–657 (2008).
2. Whittingham, M. S. Lithium batteries and cathode materials. *Chem. Rev.* **104**, 4271–4301 (2004).
3. Goodenough, J. B. & Park, K. S. The Li-ion rechargeable battery: a perspective. *J. Am. Chem. Soc.* **135**, 1167–1176 (2013).
4. Sun, Y., Liu, N. & Cui, Y. Promises and challenges of nanomaterials for lithium-based rechargeable batteries. *Nat. Energy* **1**, 16071 (2016).
5. Xu, K. Electrolytes and interphases in Li-ion batteries and beyond. *Chem. Rev.* **114**, 11503–11618 (2014).
6. Suo, L. et al. 'Water-in-salt' electrolyte enables high-voltage aqueous lithium-ion chemistries. *Science* **350**, 938–943 (2015).
7. Tan, G. et al. Burning lithium in CS_2 for high-performing compact Li_2S–graphene nanocapsules for Li–S batteries. *Nat. Energy* **2**, 17090 (2017).
8. Sun, Y. K. et al. High-energy cathode material for long-life and safe lithium batteries. *Nat. Mater.* **8**, 320–324 (2009).
9. Lin, D., Liu, Y. & Cui, Y. Reviving the lithium metal anode for high-energy batteries. *Nat. Nanotechnol.* **12**, 194–206 (2017).
10. Lu, Y., Tu, Z. & Archer, L. A. Stable lithium electrodeposition in liquid and nanoporous solid electrolytes. *Nat. Mater.* **13**, 961–969 (2014).
11. Zheng, Q., Ma, L., Khurana, R., Archer, L. A. & Coates, G. W. Structure–property study of cross-linked hydrocarbon/poly(ethylene oxide) electrolytes with superior conductivity and dendrite resistance. *Chem. Sci.* **7**, 6832–6838 (2016).
12. Ji, X. et al. Spatially heterogeneous carbon-fiber papers as surface dendrite-free current collectors for lithium deposition. *Nano Today* **7**, 10–20 (2012).
13. Bachman, J. C. et al. Inorganic solid-state electrolytes for lithium batteries: mechanisms and properties governing ion conduction. *Chem. Rev.* **116**, 140–162 (2016).
14. Miller, T. F., Wang, Z. G., Coates, G. W. & Balsara, N. P. Designing polymer electrolytes for safe and high capacity rechargeable lithium batteries. *Acc. Chem. Res.* **50**, 590–593 (2017).
15. Manthiram, A., Yu, X. & Wang, S. Lithium battery chemistries enabled by solid-state electrolytes. *Nat. Rev. Mater.* **2**, 16103 (2017).
16. Wang, Y. et al. Design principles for solid-state lithium superionic conductors. *Nat. Mater.* **14**, 1026–1031 (2015).
17. Fan, L., Wei, S., Li, S., Li, Q. & Lu, Y. Recent progress of the solid-state electrolytes for high-energy metal-based batteries. *Adv. Energy Mater.* **8**, 1702657 (2018).
18. Han, X. et al. Negating interfacial impedance in garnet-based solid-state Li metal batteries. *Nat. Mater.* **16**, 572–579 (2017).
19. Han, F., Gao, T., Zhu, Y., Gaskell, K. J. & Wang, C. A battery made from a single material. *Adv. Mater.* **27**, 3473–3483 (2015).
20. Kato, Y. et al. High-power all-solid-state batteries using sulfide superionic conductors. *Nat. Energy* **1**, 16030 (2016).
21. Christie, A. M., Lilley, S. J., Staunton, E., Andreev, Y. G. & Bruce, P. G. Increasing the conductivity of crystalline polymer electrolytes. *Nature* **433**, 50–53 (2005).
22. Zhang, J. et al. Safety-reinforced poly(propylene carbonate)-based all-solid-state polymer electrolyte for ambient-temperature solid polymer lithium batteries. *Adv. Energy Mater.* **5**, 1501082 (2015).
23. Lin, D. et al. High ionic conductivity of composite solid polymer electrolyte via in situ synthesis of monodispersed SiO_2 nanospheres in poly(ethylene oxide). *Nano Lett.* **16**, 459–465 (2016).
24. Liu, W. et al. Enhancing ionic conductivity in composite polymer electrolytes with well-aligned ceramic nanowires. *Nat. Energy* **2**, 17035 (2017).
25. Li, Y. et al. Mastering the interface for advanced all-solid-state lithium rechargeable batteries. *Proc. Natl Acad. Sci. USA* **113**, 13313–13317 (2016).
26. Han, F. et al. High electronic conductivity as the origin of lithium dendrite formation within solid electrolytes. *Nat. Energy* **4**, 187–196 (2019).
27. Tian, H. K., Xu, B. & Qi, Y. Computational study of lithium nucleation tendency in $Li_7La_3Zr_2O_{12}$ (LLZO) and rational design of interlayer materials to prevent lithium dendrites. *J. Power Sources* **392**, 79–86 (2018).
28. Fu, K. et al. Three-dimensional bilayer garnet solid electrolyte based high energy density lithium metal-sulfur batteries. *Energy Environ. Sci.* **10**, 1568–1575 (2017).
29. Harry, K. J., Hallinan, D. T., Parkinson, D. Y., MacDowell, A. A. & Balsara, N. P. Detection of subsurface structures underneath dendrites formed on cycled lithium metal electrodes. *Nat. Mater.* **13**, 69–73 (2014).
30. Xue, Z., He, D. & Xie, X. Poly(ethylene oxide)-based electrolytes for lithium-ion batteries. *J. Mater. Chem. A* **3**, 19218–19253 (2015).
31. Croce, F., Appetecchi, G. B., Persi, L. & Scrosati, B. Nanocomposite polymer electrolytes for lithium batteries. *Nature* **394**, 456–458 (1998).
32. Wang, C., Zhang, X.-W. & Appleby, A. J. Solvent-free composite peo-ceramic fiber/mat electrolytes for lithium secondary cells. *J. Electrochem. Soc.* **152**, A205–A209 (2005).

33. Fu, K. et al. Flexible, solid-state, ion-conducting membrane with 3D garnet nanofiber networks for lithium batteries. *Proc. Natl Acad. Sci. USA* **113**, 7094–7099 (2016).
34. Zhao, C.-Z. et al. An anion-immobilized composite electrolyte for dendrite-free lithium metal anodes. *Proc. Natl Acad. Sci. USA* **114**, 11069–11074 (2017).
35. Villaluenga, I. H. et al. Compliant glass–polymer hybrid single ion-conducting electrolytes for lithium batteries. *Proc. Natl Acad. Sci. USA* **113**, 52–57 (2016).
36. Zhai, H. et al. A flexible solid composite electrolyte with vertically aligned and connected ion-conducting nanoparticles for lithium batteries. *Nano Lett.* **17**, 3182–3187 (2017).
37. Zheng, J., Tang, M. & Hu, Y. Y. Lithium ion pathway within $Li_7La_3Zr_2O_{12}$–polyethylene oxide composite electrolytes. *Angew. Chem. Int. Ed.* **55**, 12538–12542 (2016).
38. Singh, V. et al. High thermal conductivity of chain-oriented amorphous polythiophene. *Nat. Nanotechnol.* **9**, 384–390 (2014).
39. Jo, G., Ahn, H. & Park, M. J. Simple route for tuning the morphology and conductivity of polymer electrolytes: one end functional group is enough. *ACS Macro Lett.* **2**, 990–995 (2013).
40. Webb, M. A. et al. Systematic computational and experimental investigation of lithium-ion transport mechanisms in polyester-based polymer electrolytes. *ACS Cent. Sci.* **1**, 198–205 (2015).
41. Sethuraman, V., Mogurampelly, S. & Ganesan, V. Ion transport mechanisms in lamellar phases of salt-doped PS–PEO block copolymer electrolytes. *Soft Matter* **13**, 7793–7803 (2017).
42. Golodnitsky, D., Livshits, E. & Peled, E. Highly conductive oriented PEO-based polymer electrolytes. *Macromol. Symp.* **203**, 27–45 (2003).
43. Toney, M. F. et al. Near-surface alignment of polymers in rubbed films. *Nature* **374**, 709–711 (1995).
44. Wang, C. et al. In situ neutron depth profiling of lithium metal–garnet interfaces for solid state batteries. *J. Am. Chem. Soc.* **139**, 14257–14264 (2017).

Acknowledgements

The work was supported by the Assistant Secretary for Energy Efficiency and Renewable Energy, Office of Vehicle Technologies of the US Department of Energy under the Battery Materials Research (BMR) programme and Battery 500 Consortium programme. Z.L. and L.-Q.C. also acknowledge the support from the Department of Energy, Office of Energy Efficiency and Renewable Energy (EERE), under the Award (DE-EE0007803).

Author contributions

J. Wan, J.X. and Y.C. designed the research. J. Wan and J.X. conducted the fabrication and electrochemical characterization of the hybrid SPE. J. Wan, J.X., K.L., F.S. and H.C. did sample characterizations. W.C., J.C., J. Wang and X.Z. helped with sample fabrication and processing. X.K. and J.Q. performed the molecular dynamics simulations and data analysis. Z.L. and L.-Q.C. performed the phase field simulations and data analysis. J. Wan, J.X., F.S., A.P. and Y.C. wrote the manuscript. All authors contributed to the discussion of the manuscript.

Competing interests

The authors declare no competing interests.

Additional information

Supplementary information is available for this paper at https://doi.org/10.1038/s41565-019-0465-3.

Correspondence and requests for materials should be addressed to Y.C.

Methods

Preparation of SPE. PEO (MW = 300,000, Sigma Aldrich) was mixed with LiTFSI (Solvay) and acetonitrile (anhydrous, Sigma Aldrich) using a Thinky mixer (Thinky Cooperation). The EO to Li ratio was 10:1. Pure PEO/LiTFSI films were prepared by doctor blade casting followed by drying in a vacuum oven at 60 °C for 24 h and baking in an Ar-filled glove box at 100 °C for at least 48 h. The porous PI films (it4ip) were fabricated from thin Kapton PI films using a track-etching technique. This technique can be generally applied to obtain aligned channels in a number of other polymer systems. PI/PEO/LiTFSI solid electrolytes were obtained in a facile two-step process. First, as-prepared PEO/LiTFSI/acetonitrile solution drops were spun at 4,000 r.p.m. with porous PI film. The as-prepared PI/PEO/LiTFSI film was then baked at 200 °C under vacuum to ensure the full infiltration of PEO/LiTFSI in the 200 nm pores. The excess PEO/LiTFSI was scraped off at 150 °C on a hot plate. The PI/PEO/LiTFSI film then underwent the same drying process as the regular PEO/LiTFSI film.

Preparation of other battery components. LFP powders (MTI), PEO/LiTFSI and carbon black (w:w:w = 60:25:15) were mixed in acetonitrile using a Thinky mixer. The LFP active material loading was 1.5 mg cm^{-2} (for high-cathode-loading results see Supplementary Fig. 24). The slurry was then doctor blade casted on Al foil. The electrode was then dried in a 60 °C vacuum oven for at least 48 h. Coin cells (2032 type, MTI) were made either with Li/SPE/Li or Li/SPE/LFP-type cells. Li foil was obtained from Sigma Aldrich.

Materials characterizations. SEM images were obtained with a FEI XL30 Sirion SEM. Mechanical tests were undertaken with a TA instrument Q800 DMA. Two-dimensional X-ray diffraction data were obtained with a Bruker D8 Venture system.

Electrochemical characterizations. Ionic conductivity measurements were conducted with a symmetrical SS/SPE/SS structure in coin cells (2032 type). Electrochemical measurements, such as electrochemical impedance spectroscopy and cycling tests, were carried out with Bio-logic VMP3 and LAND systems. All temperature-controlled experiments were tested inside an environmental chamber (BTU-133, ESPEC North America) using a high-precision thermometer (±0.1 °C).

Molecular dynamics simulations. For all molecular dynamics simulations, the optimized potentials for liquid simulations all-atom (OPLS-AA)[45] force field was used to describe PEO, Li ion and TFSI$^-$. The atomic charges of the PEO monomer were calculated using density functional theory (DFT) based on an oligomer consisting of five EO monomers. The DFT calculations used the Becke exchange plus Lee–Yang–Parr functional (B3LYP) and 6-311++g(d,p) basis sets, and were conducted using Gaussian 09 (ref. [46]). The atomic partial charges were estimated by matching the electrostatic potentials from DFT calculations. All simulations were performed using the Gromacs simulation package[47]. The equations of motion were evolved using the velocity Verlet integrator with a 2 fs time step. A cut-off of 12 Å was used to calculate both Lennard-Jones interactions and electrostatic interactions, and the particle-mesh Ewald method was used to evaluate the long-range electrostatic interactions with a grid spacing of 1.2 Å. The temperature was controlled using the Nosé–Hoover thermostat with a relaxation time of 0.2 ps. For each system, a fixed number of PEO chains, cations and anions were loaded into a simulation box with a low density (~0.1 g cm^{-3}). The system was subjected to compression in a 1 ns simulation with pressure coupled to 1,000 bar at 500 K. A further 10 ns equilibration in the NPT (constant pressure and temperature) ensemble at 1 bar, 350 K was conducted to achieve equilibrated density. To build the randomly mixed mixture, after NPT equilibration, the non-bonded interaction of the system was turned off and an NVT (constant volume and temperature) simulation was conducted for 10 ns. For the aligned PEO system, during the NVT simulation without non-bonded interactions, a force of 1,000 kJ (mol nm)$^{-1}$ was applied to both ends of each chain in opposite directions. After 50 ns equilibration in the NVT ensemble, a production run of 70 ns in the NVT ensemble was further conducted to examine ion-diffusion behaviour.

Data availability

The data that support the plots within this paper and other findings of this study are available from the corresponding author upon reasonable request.

References

45. Jorgensen, W. L., Maxwell, D. S. & Tirado-Rives, J. Development and testing of the OPLS all-atom force field on conformational energetics and properties of organic liquids. *J. Am. Chem. Soc.* **118**, 11225–11236 (1996).
46. Frisch, M. J. et al. *Gaussian 09* (Gaussian, Inc., 2009).
47. Van Der Spoel, D. et al. GROMACS: fast, flexible, and free. *J. Comput. Chem.* **26**, 1701–1718 (2005).